

## Diverse Oxygen Abundance in Early Galaxies Unveiled by Auroral Line Analysis with JWST

TAKAHIRO MORISHITA <sup>1</sup>, MASSIMO STIAVELLI <sup>2</sup>, CLAUDIO GRILLO <sup>3,4</sup>, PIERO ROSATI <sup>5,6</sup>, STEFAN SCHULD <sup>3,4</sup>,  
MICHELE TRENTI <sup>7,8</sup>, PIETRO BERGAMINI <sup>3,5</sup>, KIT BOYETT <sup>7,8</sup>, RANGA-RAM CHARY <sup>1</sup>, NICHA LEETHOCHAWALIT <sup>9</sup>,  
GUIDO ROBERTS-BORSANI <sup>10</sup>, TOMMASO TREU <sup>11</sup> AND EROS VANZELLA <sup>12</sup>

<sup>1</sup>*IPAC, California Institute of Technology, MC 314-6, 1200 E. California Boulevard, Pasadena, CA 91125, USA*

<sup>2</sup>*Space Telescope Science Institute, 3700 San Martin Drive, Baltimore, MD 21218, USA*

<sup>3</sup>*Dipartimento di Fisica, Università degli Studi di Milano, Via Celoria 16, I-20133 Milano, Italy*

<sup>4</sup>*INAF - IASF Milano, via A. Corti 12, I-20133 Milano, Italy*

<sup>5</sup>*INAF - OAS, Osservatorio di Astrofisica e Scienza dello Spazio di Bologna, via Gobetti 93/3, I-40129 Bologna, Italy*

<sup>6</sup>*Dipartimento di Fisica e Scienze della Terra, Università degli Studi di Ferrara, Via Saragat 1, I-44122 Ferrara, Italy*

<sup>7</sup>*School of Physics, University of Melbourne, Parkville 3010, VIC, Australia*

<sup>8</sup>*ARC Centre of Excellence for All Sky Astrophysics in 3 Dimensions (ASTRO 3D), Australia*

<sup>9</sup>*National Astronomical Research Institute of Thailand (NARIT), Mae Rim, Chiang Mai, 50180, Thailand*

<sup>10</sup>*Department of Astronomy, University of Geneva, Chemin Pegasi 51, 1290 Versoix, Switzerland*

<sup>11</sup>*Department of Physics and Astronomy, University of California, Los Angeles, 430 Portola Plaza, Los Angeles, CA 90095, USA*

<sup>12</sup>*INAF - OAS, Osservatorio di Astrofisica e Scienza dello Spazio di Bologna, via Gobetti 93/3, I-40129 Bologna, Italy*

(Accepted May 29, 2024)

Submitted to ApJ

### ABSTRACT

We present deep JWST NIRSpec observations in the sightline of MACS J1149.5+2223, a massive cluster of galaxies at  $z = 0.54$ . We report the spectroscopic redshift of 28 sources at  $3 < z < 9.1$ , including 9 sources with the detection of the [O III] $_{\lambda 4363}$  auroral line. Combining these with 16 [O III] $_{\lambda 4363}$ -detected sources from publicly available JWST data, our sample consists of 25 galaxies with robust gas-phase metallicity measurements via the direct method. We observe a positive correlation between stellar mass and metallicity, with a  $\sim 0.5$  dex offset down below the local relation. Interestingly, we find a larger than expected scatter of  $\sim 0.3$  dex around the relation, which cannot be explained by redshift evolution among our sample or other third parameters. The scatter increases at higher redshift, and we tentatively attribute this to the enrichment process having higher stochasticity due to shallower potential wells, more intense feedback processes, and a higher galaxy merger rate. Despite reaching to a considerably low-mass regime ( $\log M_*/M_{\odot} \sim 7.3$ ), our samples have metallicity of  $\log(\text{O}/\text{H}) + 12 \gtrsim 7$ , *i.e.* comparable to the most metal poor galaxies in the local Universe. The search of primordial galaxies may be accomplished by extending toward a lower mass and/or by investigating inhomogeneities at smaller spatial scales. Lastly, we investigate potential systematics caused by the limitation of JWST’s MSA observations. Caution is warranted when the target exceeds the slit size, as this situation could allow an overestimation of “global” metallicity, especially under the presence of strong negative metallicity gradient.

### 1. INTRODUCTION

The gas cycle within a galaxy system carries an important role. The ejecta from previously formed stars enrich surrounding gas, some fraction of which is subject to be

used in the following star formation cycles, leading to further enhancement in chemical abundances. The accumulation of stars formed in such a cyclical way represents a major component of galaxies in a later epoch, culminating with an established relation of metal contents and other fundamental galaxy properties, such as stellar mass, seen in the local universe (e.g., Tremonti et al. 2004; Gallazzi et al. 2005; Andrews & Martini

2013; Kirby et al. 2013; Curti et al. 2020). Observations have reported the presence of the relationship out to  $z \sim 3$ , but with an offset to the local relation (e.g., Maiolino et al. 2008; Zahid et al. 2011; Henry et al. 2013; Steidel et al. 2016; Sanders et al. 2021).

However, galaxies are by no means closed systems, and thus chemical enrichment on a galaxy lifetime scale is multifaceted. Star formation, ejection of enriched gas by stellar feedback and accretion of pristine gas from cosmic web have a complex interplay that ultimately defines a unique chemical enrichment history for a given object. The situation is expected to be even more complicated at earlier times, where the gas infall rate is higher, star formation is more intense, and the gravitational potential well is not deep owing to the lower mass of (proto)galaxies. As such, extending the observational frontier toward higher redshift is critical to our understanding of the origin of such a tight correlation between metallicity, which is often represented by oxygen abundance measurements, and other galaxy properties.

With the advent of JWST (Gardner et al. 2023), galaxy interstellar medium studies are now possible at  $z \gtrsim 4$  (Curti et al. 2023a; Heintz et al. 2023a; Laseter et al. 2023; Nakajima et al. 2023; Sanders et al. 2023; Stiavelli et al. 2023). The unparalleled JWST sensitivity can capture spectral features of high redshift galaxies at rest-frame optical wavelengths, such as those from oxygen and hydrogen, enabling a fair comparison to the variety of well-established lower redshift studies in the literature. Most importantly, the O/H abundance can be inferred from the electron temperature ( $T_e$ ), which in turn is measured from the ratio of the  $[\text{O III}]_{\lambda 4363}$  auroral emission line to  $[\text{O III}]_{\lambda 5007}$ . This measurement, often referred to as *direct* method, enables robust determination of oxygen abundances. In contrast, most of the pre-JWST high- $z$  studies adopt indirect metallicity inference, e.g., *R23* (Pettini & Pagel 2004; Maiolino et al. 2008; Marino et al. 2013; Curti et al. 2020). Such indirect methods are in many cases constructed and calibrated from local measurements, and thus have limitation, e.g., are applicable only within a moderate metallicity range  $\gtrsim 8$  (e.g., Curti et al. 2020). As such, their application to high- $z$  galaxies is potentially subject to systematic biases.

Auroral lines are, however, faint. For example,  $[\text{O III}]_{\lambda 4363}$  is of the order of  $\sim 1/100$  to  $[\text{O III}]_{\lambda 5007}$ , hence the direct oxygen measurement was previously limited to a smaller fraction of  $z > 0$  galaxies, and to only a handful at  $z \sim 2$ -3 (Sanders et al. 2016, 2020; Gburek et al. 2019). On the other hand,  $[\text{O III}]_{\lambda 4363}$  intensity increases as the electron temperature increases. With galaxies being less enriched and hosting more

intense star formation, the application of the direct method becomes relatively more favorable within the higher redshift range enabled by JWST.

In this study, we present our Cycle 1 GTO observations (PID 1199; Stiavelli et al. 2023), executed along the sightline of MACS J1149.5+2223, a massive cluster of galaxies at  $z = 0.54$ . We report the detection of the  $[\text{O III}]_{\lambda 4363}$  line in 9 galaxies, out of 28 sources at  $3 < z < 9.1$  spectroscopically confirmed in the program. We combine this new sample with spectroscopic data for an additional 16 galaxies with  $[\text{O III}]_{\lambda 4363}$  available in the literature, aiming to obtain robust oxygen abundance measurements of these galaxies and to investigate their relation with global properties. In Sec. 2 we present our data reduction, followed by our spectroscopic and photometric analyses in Sec. 3. We then characterize their physical properties and investigate the relationship between stellar mass and oxygen abundance in Sec. 4. We discuss the inferred properties of early galaxies in the context of galaxy evolution in Sec. 5. Where relevant, we adopt the AB magnitude system (Oke & Gunn 1983; Fukugita et al. 1996), cosmological parameters of  $\Omega_m = 0.3$ ,  $\Omega_\Lambda = 0.7$ ,  $H_0 = 70 \text{ km s}^{-1} \text{ Mpc}^{-1}$ , and the Chabrier (2003) initial mass function. Throughout the manuscript, we use the term metallicity to refer to oxygen abundance.

## 2. DATA

### 2.1. NIRSpec/MSA Spectroscopic Observations

The NIRSpec/MSA observations were configured with two medium-resolution gratings (G235M and G395M), aiming to capture rest-frame optical emission lines of galaxies at  $z \sim 3$ -9. Our NIRSpec observations were executed over four different visits. The first two visits, #20 and #22, were taken at position angle PA=257.766 degree with G235M and G395M, respectively. In the second group of visits, the same grating pair was used, but with a slightly different position angle, namely PA=259.660 degree for visit #21/G235M and PA=256.766 degree for visit #23/G395M. The total science time, excluding overhead, is 16632 sec for each grating, though not all sources have the full exposure coverage due to the mask design.

We designed a slit mask for each of the four MSA visits. The parent source catalog was constructed by using the existing HST imaging data, including CLASH, HFF, GLASS, and BUFFALO (Postman et al. 2012; Treu et al. 2015; Lotz et al. 2017; Kelly et al. 2018; Steinhardt et al. 2020). Spectroscopically redshift measurements available in the literature were also incorporated (Grillo et al. 2016; Treu et al. 2016; Shipley et al. 2018, Schuld et al., in prep). In our mask design, the highest priority

was given to JD1, a previously known spec- $z$  source at  $z = 9.1$  (Hashimoto et al. 2018; Hoag et al. 2019), followed by  $z > 6$  galaxies presented in Zheng et al. (2017) and then  $z > 1$  galaxies. The sources in our catalog were firstly identified based on the existing WFC3-IR-stack detection. However, since the NIRSpec coverage is larger than the WFC3-IR footprint, we expanded our source coverage to the ACS F606W+F814W footprint, which offers  $z \lesssim 4$  dropout sources as fillers. For each source, the default 3 shutter slitlets were assigned, enabling exposure at three positions separated for  $0.''46$  from each. We selected the default (Entire Open Shutter Area) for source allocations in APT, which secures to place the source center position within 35 milliarcsec from the shutter boundary. Including fillers and open shutters in empty sky regions, our MSA masks consisted of in total 341 unique sources.

For the MSA data reduction, we use `msaexp`<sup>1</sup> following Morishita et al. (2023). The one-dimensional spectrum is extracted via optimal extraction. The source light profile along the cross-dispersion direction is directly measured using the 2-d spectrum. For sources with faint continuum or with any significant contamination (i.e. from a failed open shutter), we visually inspect the 2-d spectrum and manually define the extraction box along the trace where any emission lines are identified.

## 2.2. Imaging Data Reduction and Photometry

NIRCam imaging observations were executed on June 6 – 8 2023 as part of the same program (Visit #5), with six filters configured (F115W, F150W, F200W, F277W, F356W, and F444W) with the MEDIUM8 readout mode, totaling in  $\sim 1.1$  hr on-source exposure in each filter.

We follow the same steps for JWST image reduction presented in Morishita & Stiavelli (2023). Briefly, we retrieve the raw-level images from the MAST archive and reduce those with the official JWST pipeline (ver.1.10.0, with `jwst_1100.pmap`), with several customized steps including  $1/f$ -noise subtraction and snowball masking. The final drizzled images are aligned with the same WCS coordinate as for the HST images, with the pixel scale set to  $0.''03$ . In Fig. 1, we show the NIRCam and NIRSpec coverage, on top of the footprint of the existing HST images.

We identify sources in the detection image using SExtractor (Bertin & Arnouts 1996), and measure their fluxes on the psf-matched mosaic images with a fixed aperture of radius  $r = 0.''16$ . The measured aperture-based fluxes of each source is then scaled by a single fac-

tor, defined as  $\text{flux}_{\text{auto},F444W}/\text{flux}_{\text{aper},F444W}$ , to the total flux. With this approach, colors remain as those measured in the aperture, whereas the fluxes are scaled to the total quantities for subsequent analysis (i.e. derivation of stellar mass and star formation rate).

## 3. ANALYSIS

### 3.1. Emission Line Fitting

As shown in Fig. 1, the slit positions for some sources do not necessarily match in the two grating observations. To accommodate potential systematic errors due to this, we correct for aperture losses. For each grating spectrum of each source, we apply a global scale factor that is derived by comparing the continuum spectrum (with the wavelengths of strong emission lines being masked) to the best-fit spectral template from our spectral energy distribution (SED) analysis (Sec. 3.3).

We then model the line profile of each emission line of interest in the extracted 1d spectrum with a Gaussian function. Our basic strategy is to define a wavelength window for each line, model the underlying continuum spectrum by a polynomial fit, and subtract it from the 1-d spectrum before the Gaussian fit is carried out. The model includes amplitude, line width, and redshift parameters. However, when multiple lines are located close to each other in wavelength, we fit those simultaneously using a common redshift parameter, so blending can effectively be resolved. In addition, doublet lines (i.e.  $[\text{O III}]_{\lambda\lambda 4959+5007}$  and  $[\text{N II}]_{\lambda\lambda 6548+6583}$ ) are modelled with a fixed line ratio (1:3 and 1:1.7, respectively), with single line width and redshift parameters. The total flux of the doublets estimated in this way remains robust, while we note that the ratio could have a systematic uncertainty  $\lesssim 10\%$  (e.g., Storey & Zeippen 2000).

The integrated flux of each line is estimated by summing the corresponding Gaussian component, and the flux error is estimated by summing the error weighted by the amplitude of the Gaussian model in quadrature. The uncertainty associated with the modeled continuum is also added. In the following analysis, we adopt flux measurements when the line is detected (signal-to-noise ratio  $S/N \geq 3$ ); for those not detected, we adopt the  $3\text{-}\sigma$  upper limit.

### 3.2. Direct Metallicity Measurements

In general, the line intensity we measure needs to be corrected for dust absorption. We determine the correction on the basis of the ratio of the strongest Balmer lines we measure, thus,  $\text{H}\alpha/\text{H}\beta$  is considered before  $\text{H}\beta/\text{H}\gamma$ . We require the Balmer lines to be detected at  $5\text{-}\sigma$  in order to apply such correction. In the absence

<sup>1</sup> <https://github.com/gbrammer/msaexp>

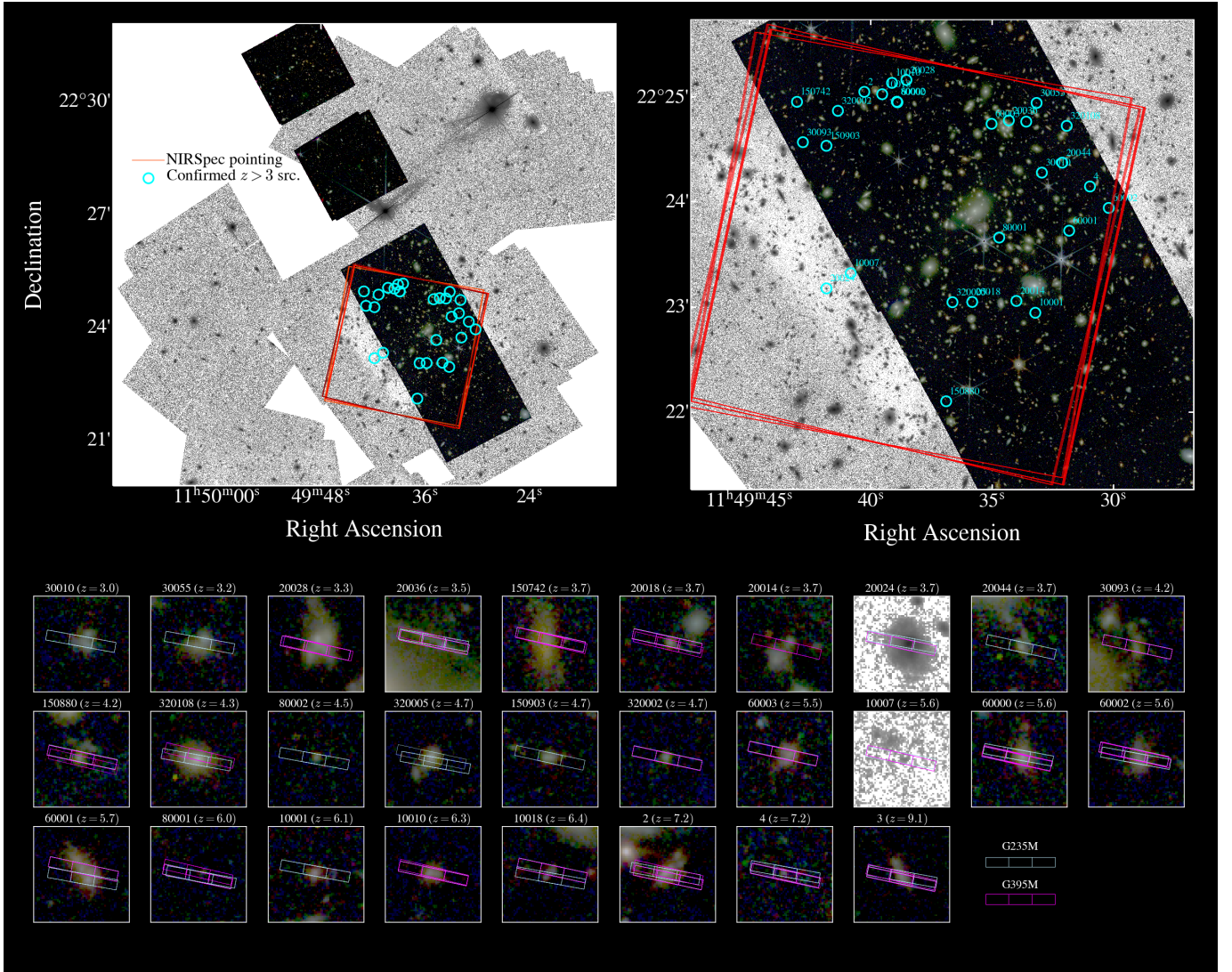


**Figure 1.** (Left): Pseudo RGB images of NIRC2 in the cluster pointing and the parallel field are shown (F115W+F150W/F200W+F277W/F356W+F444W for blue/green/red). The confirmed  $z > 3$  sources in our program are marked (cyan). The HST/ACS images are shown in the background. The Hubble Frontier Field’s parallel pointing is located to the South of the image (not shown here). NIRS2 footprints are marked (red solid rectangles). (Right): Zoomed view around the NIRS2 FoV. (Bottom): Cutout RGB stamps of  $z > 3$  sources are shown ( $2'' \times 2''$ ). The positions of MSA shutters are overlaid.

of a high S/N detection of Balmer lines, we apply no correction. Generally, we find the  $A_V$  values derived from the Balmer line ratios to be in broad agreement with the SED-derived  $A_V$  values, after using the [Calzetti \(1997\)](#) rescaling factor that accounts for continuum and emission lines dust effects.

The auroral line  $[\text{O III}]_{\lambda 4363}$  provides a reliable method to derive the electron temperature and, from that, the oxygen metallicity by using the [Izotov et al. \(2006\)](#) iterative method. The method requires knowledge of the electron density,  $n_e$ , which we cannot derive directly for (most of) the objects in our sample. In our derivation we assume  $n_e = 300 \text{ cm}^{-3}$ . We have estimated the effect of

the density uncertainty by assuming also  $n_e = 100, 1000$  to assess the range of variability. Usually this contribution to the overall uncertainty is small (but see below). The calculations require a well measured Hydrogen recombination line, ideally  $\text{H}\beta$ , which is close in wavelength to  $[\text{O III}]_{\lambda 5007}$ . For some objects the line is not measured at  $\text{S/N} \geq 3$ ; in those cases we estimate  $\text{H}\beta$  from another Balmer line using Case B ([Osterbrock & Ferland 2006](#)) and 10,000 K, assuming no attenuation. For 20018, 60001, 80001, and m39 we estimate  $\text{H}\beta$  from  $\text{H}\gamma$ , while for 80002 we estimate it from  $\text{H}\delta$ .

For objects with  $[\text{O II}]$  detection we add the contribution of singly ionized Oxygen to the total Oxygen

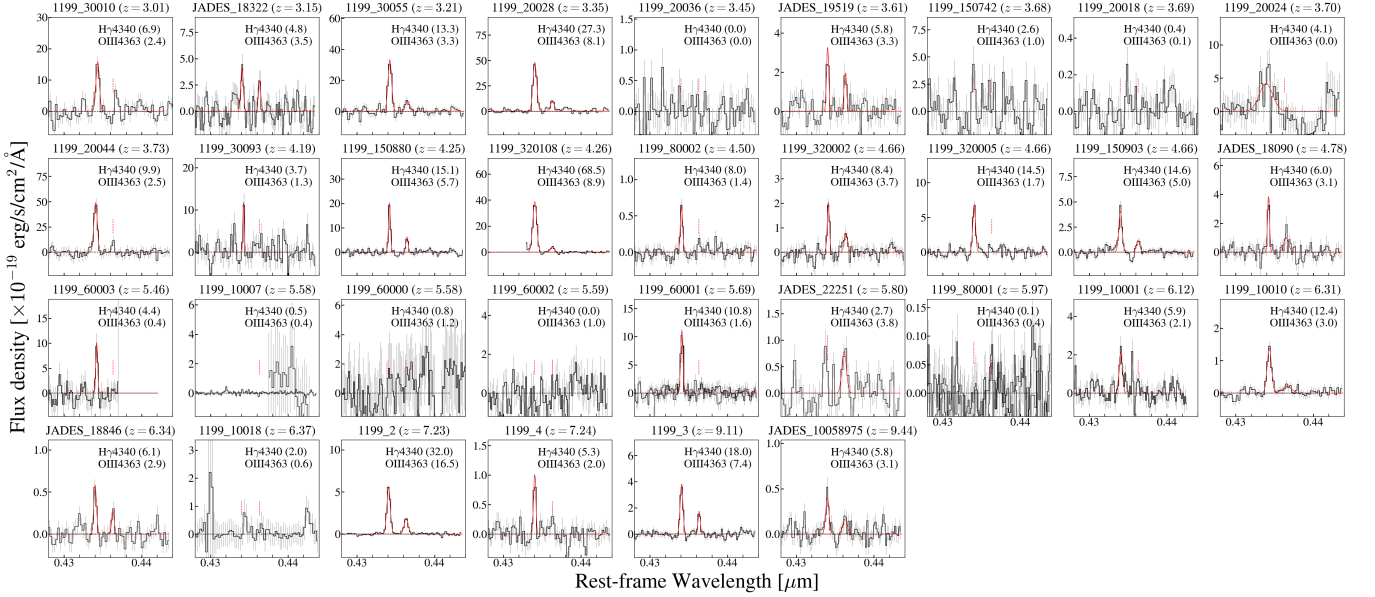


**Figure 2.** NIRSpec MSA spectra of our primary sample galaxies, zoomed in the wavelength region of the  $H\gamma$  and  $[O\text{ III}]\lambda_{4363}$  lines. The modelled gaussian is shown when the line is detected at  $> 3\text{-}\sigma$  (red solid lines). The detection significance for each line is shown in the label. Note that sources from Nakajima et al. (2023) are not shown, as we adopt their published flux measurements.

abundance by estimating the  $O^+$  temperature following Campbell et al. (1986), and then follow Izotov et al. (2006) to get the  $O^+$  abundance for the estimated temperature. These correction are always less than 0.17 and usually less than 0.1 in  $\log(O/H)+12$ . We found similar  $O^+$  temperatures in most cases when we followed Izotov et al. (2006) instead of Campbell et al. (1986). However, the polynomial fit that Izotov et al. (2006) provide was optimized for the  $O^{++}$  temperature of  $< 2 \times 10^4$  K and starts returning unrealistic values at higher temperatures. We therefore decided to adopt Campbell et al. (1986) for the  $O^+$  temperature estimate.

We derive Oxygen metallicity for objects with a  $3\text{-}\sigma$  or higher S/N for  $[O\text{ III}]\lambda_{4363}$ . For the remaining objects we adopt a value of  $[O\text{ III}]\lambda_{4363}$  identical to three times the error as an upper limit, which gives us a lower limit to the metallicity.

The derived temperatures are reported in Table 3. We find that some sources have considerably high temperature,  $\gtrsim 2 \times 10^4$  K, including 320002 ( $T_e = 2.6 \times 10^4$  K) from GTO1199. Interestingly, all JADES sources are at  $\gtrsim 2 \times 10^4$  K. While the reason for this is not clear, Laseter et al. (2024) also reported similarly high temperatures for overlapping sources.

We note that the line ratio  $I_{4363}/I_{5007}$  become much less sensitive to temperature in high electron density ISM,  $n_e \gtrsim 10^4 \text{ cm}^{-3}$ , making our direct method less validated. Indeed, recent observations reported high ( $\sim 10^5 \text{ cm}^{-3}$ ) values in two high- $z$  galaxies (Senchyna et al. 2023; Topping et al. 2024). However, we consider that

such high  $n_e$  is unlikely in most of our galaxies. Reddy et al. (2023) reported an increasing trend of  $n_e$  with star formation rate surface density,  $\Sigma_{\text{SFR}}$ . Following their derived slope ( $n_e \propto \Sigma_{\text{SFR}}^{0.51}$ ), we find electron density should remain to  $< 10^4 \text{ cm}^{-3}$ , even for an extreme case with  $\Sigma_{\text{SFR}}$  of  $\sim 10^2 M_\odot \text{ kpc}^{-3}$  (cf. Morishita et al. 2024). Isobe et al. (2023) also found that  $n_e$  of their galaxies at  $z = 6\text{-}10$  is  $< 10^4 \text{ cm}^{-3}$ .

### 3.3. Spectral Energy Distribution Analysis

We infer the spectral energy distribution (SED) of our sample galaxies through SED fitting using the JWST+HST photometric data. We use the SED fitting code `gsf` (ver1.85; Morishita et al. 2019), which allows flexible determinations of the SED by adopting binned star formation histories (often referred to as *non-parametric*). We follow the same procedure as described in Stiavelli et al. (2023), but this time without fitting spectroscopic data simultaneously as continuum fluxes of a large fraction of the sources are too faint to be useful.

The star-formation rate of individual galaxies is calculated with the rest-frame UV luminosity ( $\sim 1600 \text{ \AA}$ ) using the determined SED model. The UV luminosity is corrected for dust attenuation using the  $\beta_{\text{UV}}$  slope, which is measured by using the posterior SED, as in Smit et al. (2016):

$$A_{1600} = 4.43 + 1.99 \beta_{\text{UV}} \quad (1)$$

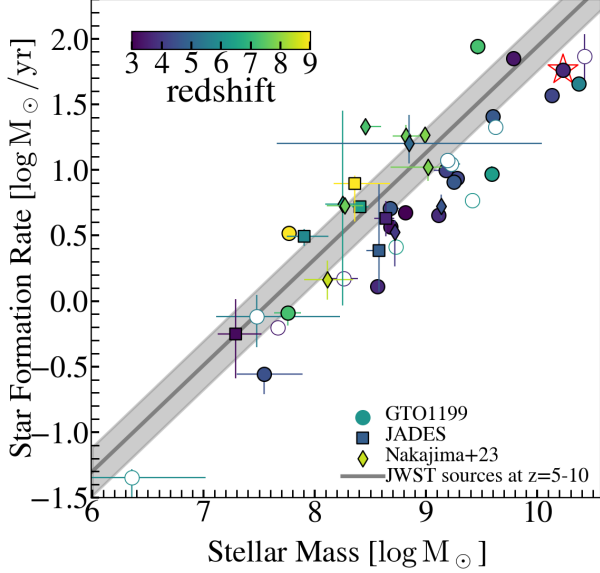


**Figure 3.** Our samples in the stellar mass–star formation rate plane. Symbols are color-coded by redshift. Different symbols represent references (circles for GTO1199, squares JADES, diamonds Nakajima et al. 2023). The linear relation derived for UV-selected galaxies at  $5 < z < 10$  (Morishita et al. 2023, solid line) is shown for comparison. The broad line object, 20024, is marked separately (red star). Those excluded from the mass-metallicity relation analysis (Sec. 4.3) are shown as open circles.

The attenuation corrected UV luminosity is then converted to SFR via the relation in Kennicutt (1998):

$$\text{SFR} [M_{\odot} \text{ yr}^{-1}] = 1.4 \times 10^{-28} L_{\text{UV}} [\text{erg s}^{-1} \text{ Hz}^{-1}]. \quad (2)$$

## 4. RESULTS

### 4.1. Spectroscopic Sample from GTO 1199

In Fig. 1, we present the cutout images of 28 sources confirmed to  $z > 3$  in the GTO1199 observations. The fluxes are reported in Table 1. We note that redshift of all sources is measured by multiple lines, in most cases including the  $[\text{O III}]$ -doublet.

Among the confirmed sources, 9 have  $\gtrsim 3\sigma$  detection in  $[\text{O III}]_{\lambda 4363}$ , with ID 3 (JD1) holding the highest redshift,  $z = 9.11$  (Stiavelli et al. 2023). The  $[\text{O III}]_{\lambda 4363}$  line of each source is shown in Fig. 2. Two sources do not have wavelength coverage for  $[\text{O III}]_{\lambda 4363}$ , due to the wavelength range falling in a detector gap or not being covered by the corresponding grating.

We note the observed high  $[\text{O III}]_{\lambda 4363}/[\text{O III}]_{\lambda \lambda 4959+5007}$  ratio for our samples, with the median value of  $\sim 0.027$  (also Sec. 5.4). This is considerably higher compared to those reported in lower- $z$  studies — for comparison, we find  $\sim 0.01$  in the Sloan sample for the mass range

of  $10^8 < M_*/M_{\odot} < 10^9$  in the MPA-JHU catalog<sup>2</sup>; Sanders et al. (2016) reported  $0.013 \pm 0.003$  for a galaxy at  $z = 3.08$ .

Overall, our sample galaxies are characterized by narrow lines. Their location on the stellar mass-SFR plane is shown in Fig. 3. The exception is ID 20024, which has broad features in Hydrogen recombination lines. This source, however, shows no significant detection of  $[\text{O III}]_{\lambda 4363}$ , and thus it is not included in our primary metallicity analysis below. The derived physical properties of our samples are reported in Table 2.

### 4.2. Additional $[\text{O III}]_{\lambda 4363}$ Samples

In addition, we explore public datasets to expand the sample size of  $[\text{O III}]_{\lambda 4363}$  sources. We include 6 galaxies at  $3 < z < 9.5$  from the JADES program (Hainline et al. 2023; Bunker et al. 2023; Eisenstein et al. 2023) observed in their medium resolution spectroscopy and 10 at  $4 < z < 8.6$  from Nakajima et al. (2023).

For the JADES sources, we start with the public 1-dimensional spectra and repeat the same line fitting analysis as for the GTO1199 sources. The measured fluxes are reported in Table 1. Four of the JADES sources were previously reported in Laseter et al. (2024). One of the Laseter et al. (2024) sources has a solid detection of  $[\text{O III}]_{\lambda 4363}$ , but has no spectroscopic coverage for the  $[\text{O III}]_{\lambda \lambda 4959+5007}$ -doublet (NIRSpec ID 00008083); as such, this source was excluded from our metallicity analysis.

For the sources reported in Nakajima et al. (2023, from public JWST fields, ERO (Pontoppidan et al. 2022), GLASS (Treu et al. 2023), and CEERS (Finkelstein et al. 2023)), we adopt their published measurements for line fluxes and magnification.

To guarantee a uniform analysis, we derive oxygen abundances using the same method presented in Sec. 4.1, and stellar mass and star formation rate as in Sec. 3.3. The derived physical properties are summarized in Table 2. We find overall good agreement of the derived abundances with the previous studies. This provides an independent verification of our method. It also enables a fair internally-consistent comparison with the objects from those studies.

### 4.3. Stellar Mass – Metallicity Distribution of Galaxies at $3 < z < 9.5$

In the left panel of Fig. 4, we show the distribution of our sample galaxies in the stellar mass-metallicity plane. Despite a wide redshift range, our samples overall distribute around the linear relation reported in the liter-

<sup>2</sup> [https://www.sdss4.org/dr17/spectro/galaxy\\_mpa\\_jhu/](https://www.sdss4.org/dr17/spectro/galaxy_mpa_jhu/).

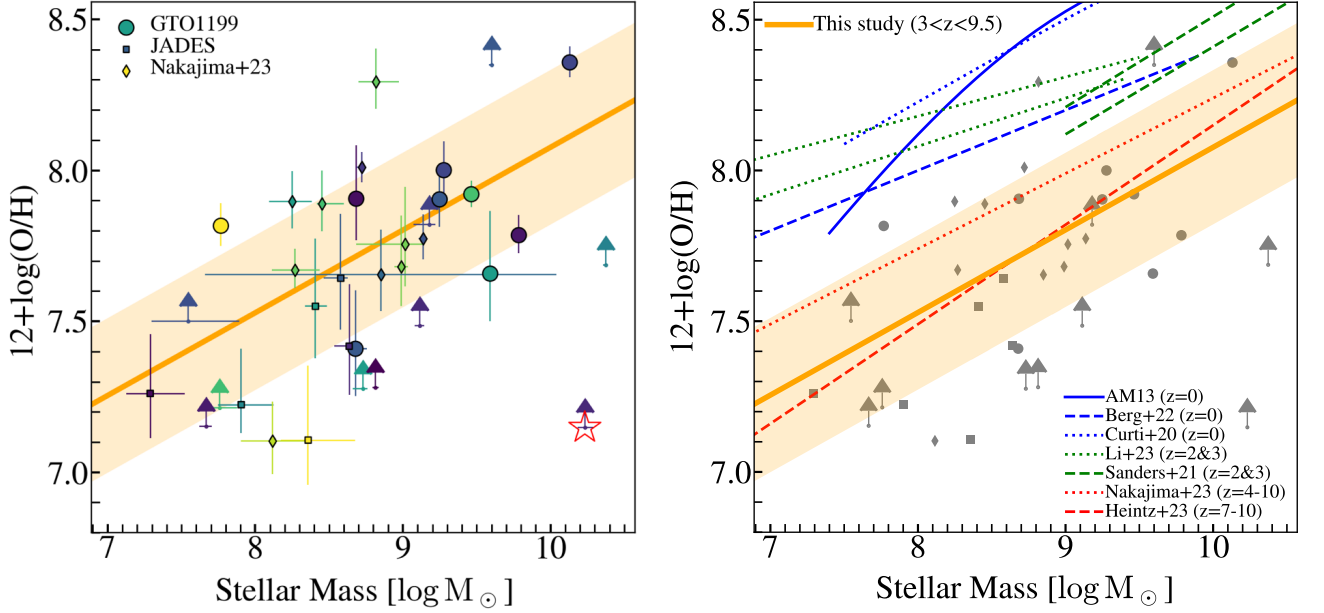


**Figure 4.** (Left): Our sample galaxies in the stellar mass–metallicity plane. Symbols and colors are the same as in Fig. 3. Those with an upper limit in  $[\text{O III}]_{\lambda 4363}$  are shown as a lower limit in  $\log(\text{O}/\text{H})$ . The best-fit slope to our sample is shown (orange solid line, with hatched regions for the  $3\text{-}\sigma$  range). (Right): Same as in the left panel, but with the mass-metallicity relation slopes determined at  $z \sim 0$  (Andrews & Martini 2013; Curti et al. 2020; Berg et al. 2022),  $z \sim 2\text{--}3$  (Sanders et al. 2021; Li et al. 2023), and high- $z$  (Heintz et al. 2023a; Nakajima et al. 2023) in the literature.

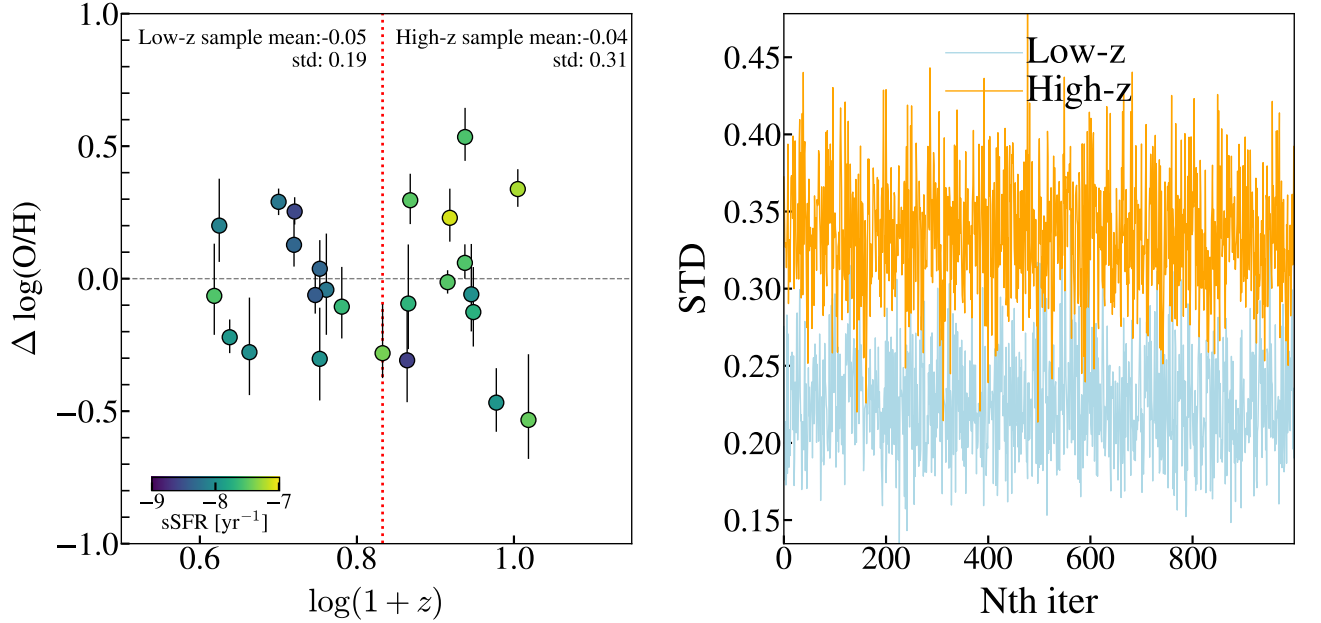


**Figure 5.** (Left): Redshift distribution of  $\Delta \log(\text{O}/\text{H})$ , metallicity offset from the determined mass-metallicity relation in Fig. 4. The mean and standard deviation are shown for each of low- and high-redshift sub-samples, split at the median redshift (vertical dotted line). Symbols are color-coded by specific star formation rate. Note that the lower limit samples are not shown. (Right): Distributions of standard deviation for low- $z$  (cyan) and high- $z$  samples (orange). Standard deviation was calculated at each iteration with random Gaussian noise for the observed uncertainties being added.

ature, derived for  $z > 3$  galaxies (Heintz et al. 2023b; Nakajima et al. 2023).

We investigate the distribution of our samples by using the following formulae:

$$12 + \log(\text{O}/\text{H}) = \alpha \log(M_*/M_0) + B(z) + N(0, \sigma_{\log\text{MZR}}), \quad (3)$$

$$B(z) = \beta_z + \alpha_z \log(1+z), \quad (4)$$

where  $N(0, \sigma_{\log\text{MZR}})$  represents a normal distribution with  $\sigma_{\log\text{MZR}}$  being the intrinsic scatter around the relationship. For the calculation of posterior distributions, we employ the Markov chain Monte Carlo method by using `emcee` (Foreman-Mackey et al. 2014). The likelihood function is defined as:

$$\ln\mathcal{L} = -0.5 \left( \sum_i (\Delta_i^2 + \ln(2\pi\sigma_i^2)) - 2\chi_{lim} \right), \quad (5)$$

where  $i$  runs through detected sources (i.e.  $\text{S/N} [\text{O III}]_{\lambda 4363} > 3$ ).  $\Delta_i$  is the normalized residual:

$$\Delta_i = (\log(\text{O}/\text{H})_{\text{model}} - \log(\text{O}/\text{H})_i) / \sigma_i. \quad (6)$$

The term of  $\chi_{lim}$  accounts for the likelihood of lower-limit sources (also, Sawicki 2012):

$$\chi_{lim} = \sum_j \ln \left( \sqrt{\frac{\pi}{2}} \sigma_j \left( 1 + \text{erf} \left( \frac{\log(\text{O}/\text{H})_{\text{model}} - \sigma_j}{\sqrt{2}\sigma_j} \right) \right) \right) \quad (7)$$

where  $j$  runs through lower-limit sources,  $\sigma_j$  lower limit on  $\log(\text{O}/\text{H})$ , and  $\text{erf}$  the error function.

We adopt the median mass of the sample as the pivot mass,  $M_0$ . From the regression analysis, we find the slope  $\alpha = 0.27 \pm 0.10$ , similar to Nakajima et al. (2023). We find a slightly smaller offset ( $\sim -0.15$  dex) from the Nakajima et al. (2023)’s relation, but the scatter around our determined relationship is considerably large ( $\sigma_{\log\text{MZR}} = 0.26 \pm 0.05$ ).

The derived intercept is  $\sim 0.4$ – $0.7$  dex lower than that in the local relation at the pivot mass,  $\log M_0 = 8.8$  (e.g., Andrews & Martini 2013; Curti et al. 2020; Berg et al. 2022, among those adopt the direct  $[\text{O III}]_{\lambda 4363}$  method). This indicates evolution of the relation, from  $z \sim 3$ – $9$  to  $z \sim 0$ , supporting the previous conclusion reported in various studies at similar redshifts (e.g., Nakajima et al. 2023; Heintz et al. 2023b).

On the other hand, redshift evolution of metallicity among our sample galaxies is not observed. The relevant parameter,  $\alpha_z$ , is consistent with no evolution (i.e.  $\alpha_z = 0.0 \pm 0.5$ ) in our regression analysis. Indeed, we find that our samples are distributed in a fairly wide range of metallicity regardless of redshift. For example, the two

highest redshift sources (JD1 and 10058975) have distinct values ( $\log(\text{O}/\text{H}) + 12 = 7.81$  and  $7.08$ ). ERO 6355 at  $z = 7.655$  is one of the most enriched galaxies in the combined sample, with  $\log(\text{O}/\text{H}) + 12 = 8.29$ . We investigate the observed scatter in Sec. 5.2.

It has been known that at lower redshifts mass-metallicity relations have dependency on a third parameter, such as SFR (e.g., Andrews & Martini 2013) and gravitational potential (e.g., Sánchez-Menguiano et al. 2023). However, none of those quantities offers significant reduction in the observed scatter. For example, with  $M_*/\text{SFR}^{0.66}$  (i.e. the fundamental-metallicity; Andrews & Martini 2013; Curti et al. 2020; Li et al. 2023), we only find a comparable intrinsic scatter,  $\sigma_{\log\text{MZR}} = 0.28$ .

To understand the observed scatter, we investigate  $\Delta \log(\text{O}/\text{H})$ , the deviation of metallicity from the determined relation, by correlating it with a third parameter. We find that when correlated with sSFR, the Pearson’s  $r$  value is 0.10 with a corresponding  $p$ -value of 0.64, indicating a lack of correlation. Similarly, we do not observe significant trends with other parameters, including SFR ( $r = 0.07$  and  $p = 0.74$ ),  $\Sigma_{\text{SFR}}$  ( $-0.26, 0.21$ ), gravitational potential ( $-0.26, 0.21$ ), stellar mass surface density ( $-0.26, 0.21$ ), light-weighted age ( $-0.26, 0.21$ ), and UV slope  $\beta$  ( $0.07, 0.74$ ).

## 5. DISCUSSION

### 5.1. On the presence of the Mass-Metallicity relation

We have observed correlation between stellar mass and metallicity for our sample galaxies. Despite the large scatter, the presence of a positive slope indicates that stellar mass formation plays a critical role in enrichment process already at these redshifts.

The observed slope of our galaxies is offset from the local relation for  $\sim 0.4$ – $0.7$  dex, depending on the local reference. A similar offset is reported in other studies at similar redshifts (e.g., Heintz et al. 2023b), and at  $z \sim 3$  (e.g., Sanders et al. 2020; Curti et al. 2023b), the lower bound of our redshift range. In contrast, we find no clear evidence of redshift evolution among our sample. We note that the time difference is much smaller at  $3 < z < 9$  ( $\sim 1.5$  Gyr; whereas  $\sim 10$  Gyr from  $z \sim 3$  to 0), while some studies reported the presence of weak evolution using a sample of calibrated metallicity (e.g., Curti et al. 2023b).

One possible interpretation is that what regulates metallicity changes around  $z \sim 2$ – $3$ , from bursty to more continuous star formation (e.g., Asada et al. 2024). At higher  $z$ , the relevant “clock” is driven by mass, rather than the specific redshift, and galaxies will enrich until perhaps an outflow quenches star formation or ejects

metals. At decreasing redshift, the star formation history becomes more important, as galaxies begin retaining metals or perhaps accreting metal rich gas so their metallicity can be higher for a given mass. It remains surprising that slopes remain similar across the cosmic time.

The absence of redshift evolution at  $z \gtrsim 5$  is reported in numerical simulations. Ucci et al. (2023) reported a decrease of metallicity for  $\log M_*/M_\odot \sim 7$  galaxy systems at decreasing redshift. They attribute this to various factors, including the differential impact of feedback in different halo mass systems at low and high redshifts. The impact by feedback becomes smaller at a larger mass system, making the “observed” evolution insignificant. Similarly weak/no redshift evolution of the relation is also reported in other numerical work (e.g., Ma et al. 2016; Langan et al. 2020).

### 5.2. On the scatter around the Mass-Metallicity relation

We have found a considerably large scatter around the determined relation. Our regression analysis above concluded that the scatter cannot be attributed to a third quantity, including the redshift dependence of the relation. For comparison, at  $z \sim 0$  the scatter is found to be  $\sim 0.1$  around the fundamental mass-metallicity relation at the same mass range (Curti et al. 2020).

While we discuss observational systematics that may attribute to the scatter in Section 5.3, here we focus on potential attributes arising from the nature of our sample galaxies. The large scatter could be interpreted that metal enrichment process occurs rapidly, but also susceptible to mechanisms that dilute the enrichment over a similar time scale. Such inverse processes are expected to be less significant at lower redshift, where a stronger gravitational potential aids retaining the enriched gas within the galaxy system against feedback processes. We note that in the stellar mass range of interest here, the halo mass of the system increases as redshift decreases until  $z \sim 1$  (and then it decreases toward  $z \sim 0$ ; e.g., Behroozi et al. 2019).

Our data supports the interpretation. In Fig. 5, we show  $\Delta \log(\text{O}/\text{H})$  as a function of redshift. Clearly, the amplitude of the scatter increases at increasing redshift. The standard deviation for the lower-half and higher-half redshift samples are  $0.17 \pm 0.04$  and  $0.28 \pm 0.07$ , respectively. Since the sample size is not large, we adopt a simple Gaussian estimator and bootstrap method to derive the quoted uncertainty (Beers et al. 1990, also Morishita et al. 2023). We have also confirmed the result through an iterative approach, where the standard

deviation with scatter added to the metallicity measurements at each iteration (Fig. 5, right panel).

Notably, high- $z$  galaxies are intense in star formation. In Morishita et al. (2023), we reported that star formation rate surface density,  $\Sigma_{\text{SFR}}$ , of  $z > 5$  galaxies is  $\sim 10$ – $100$  times higher than  $z \sim 2$  samples, driven both by compact morphology and high star formation rate. The decrease of scatter amplitude can be explained such that interplay between the potential well and feedback process becomes more constrained at decreasing redshift.

We remind the absence of clear correlation between  $\Delta \log(\text{O}/\text{H})$  and sSFR in our sample. The lack of correlation with sSFR could simply be due to the fact that chemical enrichment may not necessarily proceed in the same time scale for star formation at these redshifts ( $\lesssim 200$  Myr; Faisst & Morishita 2024).

Alternatively, an increased fraction of merger-driven evolution would also explain the observed trend of the scatter with redshift. As redshift increases, so does the merger rate (Fakhouri & Ma 2008, also Hsiao et al. 2023; Boyett et al. 2024; Dalmasso et al. 2024), and thus galaxy assembly is progressively more driven by mergers than smooth accretion, though the actual merger rate for low-mass galaxies at these redshifts is yet to be observationally constrained. As a result, the system’s chemical enrichment is more affected by independent building blocks rather than by smooth accretion of material and self-recycling.

Simulations find a different conclusion. Ucci et al. (2023) reported a dependence of the relationship on specific star formation rate at  $z > 5$ , in a way that a lower metallicity galaxy has a higher sSFR. Their observed trend is interpreted as the strong star formation could blow the enriched gas away from the system, while pristine gas may still feed the galaxy system. We do not observe this trend in our sample. A larger sample may be needed to confirm the predictions.

### 5.3. Potential Systematic Uncertainties

Slit-spectroscopy observations have two major limitations, namely the position of slit regarding the galaxy center and aperture loss due to the limited slit size. Since the mass-metallicity relation concerns the global metallicity of the system, those systematic uncertainties need to be addressed. Those effects are particularly the case for JWST for its design of MSA masks, its resolving power, and its relatively small size of the slit ( $0.''2 \times 0.''46$ ). Despite its critical importance, the literature has not yet engaged in a comprehensive discussion on these systematic issues.

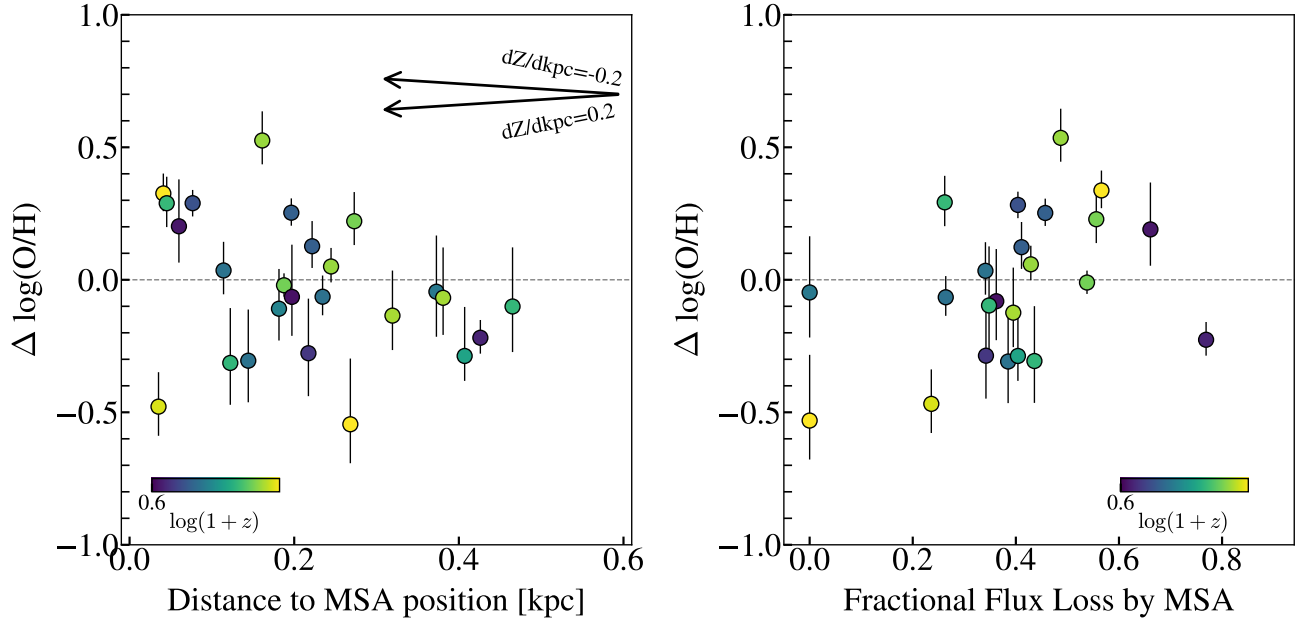


**Figure 6.** Same as Fig. 5, but with different quantities for the  $x$ -axis. (Left): Distance from the MSA shutter position to the light-weighted center of the target galaxy. The distribution of our samples does not reveal a clear trend with the offset amplitude. The deviation from the mean relation cannot be explained by the offset, even under the presence of steep metallicity gradient (0.2 dex/kpc and  $-0.2$  dex/kpc; arrows). (Right): Fractional flux loss of MSA (i.e. flux that falls out of the MSA slit over the total flux). The fraction flux loss estimated in F444W is shown here.

In our observations, we find that several targets show a small offset in the MSA slit position from its light center (Fig. 1). This is partially due to our selection of “Entire Open Shutter Area” configuration in APT, chosen to maximize multiplexity, leading to an offset of  $\sim 0.25$  arcsec at maximum. Such an offset would have no impact to mass-metallicity relation if the metallicity measured at the position represents the entire system. However, this is not necessarily the case. Studies have found a pronounced gradient in gas-phase metallicity in active galaxies, up to  $z \sim 3$  (e.g., Belfiore et al. 2017; Bresolin 2019; Wang et al. 2020).

We investigate this by examining the deviation in metallicity from the mean relationship in relation to the offset distance (Fig. 6, left). Our analysis reveals no clear indication that the offset amplitude is the primary cause for the observed scatter. In fact, the observed scatter amplitude surpasses what can be accounted for by an extreme gradient reported in the literature ( $\pm 0.2$  dex/kpc). Recent observations revealed negative metallicity gradient in galaxies of similar redshifts (Arribas et al. 2023; Vallini et al. 2024), while the scatter is likely more significant due to shorter mixing timescales of gas-phase metallicity (e.g., Venturi et al. 2024).

We then investigate the impact by aperture loss. We here measure fractional aperture loss ( $\Delta f_{\text{MSA}}$ ), i.e. flux

that falls out of the slit over the total flux of the target, in the F444W image. The right panel of Figure 6 shows the distribution. This quantity ranges from  $\sim 0$  (i.e. most flux is within the slit) to 0.8 (20% is within the slit) for our sample, with the median value 0.4. Interestingly, three sources that are least affected by the loss ( $\Delta f_{\text{MSA}} < 0.25$ ) have metallicity below the mean relation. On the other hand, at the high-loss end ( $\Delta f_{\text{MSA}} \gtrsim 0.5$ ), four (3, 30055, ERO\_6355, GLASS\_10021) out of six are located above the mean metallicity relation.

Despite the observed signal being statistically weak, this reveals an important implication. Since the MSA slit position is, in default, configured to be near the light center of the target, the inferred metallicity would be biased to the central part, where metallicity is likely most enriched. The effect would become significant when there exists a negative gradient *and* the aperture loss is large (i.e. large-sized target), leading to an overestimated metallicity. In other words, the four sources of high  $\Delta f_{\text{MSA}}$  may be observed to be metal rich *because* their low-metallicity part might have fallen out of the slit. Qualitatively, the impact should remain  $\lesssim 0.2$  dex reduction in metallicity at most for the typical apparent size of our galaxies assuming a gradient of  $-0.2$  dex/kpc. A more realistic estimate could be achieved upon the

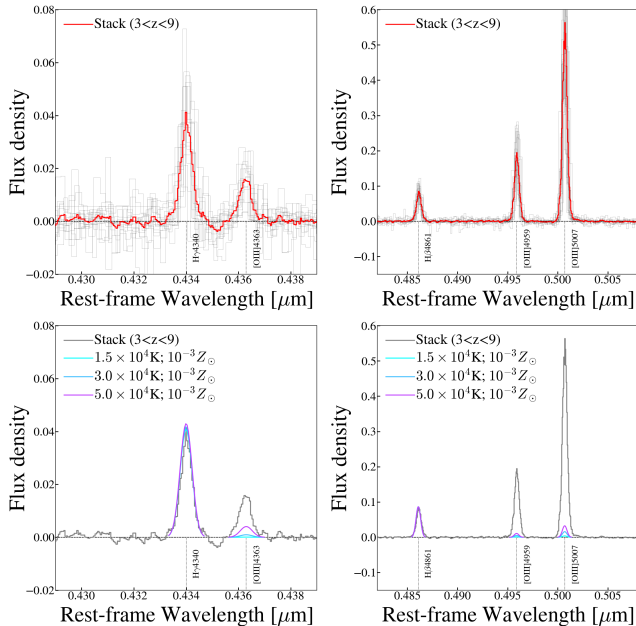


**Figure 7.** (Top panels): Stacked spectrum of the sample galaxies that have  $[\text{O III}]_{\lambda 4363}$  detected (red lines). Individual spectra are shown in the background (gray lines). All spectra were subtracted continuum and normalized by the integrated  $\text{H}\beta$  line flux before being stacked. (Bottom panels): Same stacked spectra are shown (gray), along with three metal-poor models of for different temperatures ( $1.5, 3,$  and  $5 \times 10^4$  K, with  $Z = 10^{-3} Z_{\odot}$ ).

consideration of, e.g., the actual light profile and metallicity gradient, which is beyond the scope of this study.

We also repeat the regression analysis but this time with 24 galaxies with those fractional flux loss  $< 0.5$ . We do not see decrease in the scatter ( $\sigma_{\log \text{MZR}} = 0.27$ ; Table 3). We find positive redshift evolution of the intercept, but the significance remains too tentative to confirm the trend ( $\alpha_z = -0.3 \pm 0.7$ ).

#### 5.4. Toward the identification of Pop-III galaxies

Through the robust determination of oxygen abundance, our data reveal the distribution of early galaxies in the mass-metallicity plane. Despite probing a wide range of both redshift and stellar mass, our galaxies turn to be moderately enriched in metallicity,  $\log(\text{O}/\text{H})+12 \gtrsim 7$ . For comparison, the prototype of low-metallicity galaxy in the local Universe, I Zw 18, has  $\log(\text{O}/\text{H})+12 = 7.17$  (Izotov et al. 1999). The lowest mass galaxy among our mass-metallicity relation sample, with  $\log M_*/M_{\odot} = 7.3$  (ID 18322), has oxygen abundance of  $\log(\text{O}/\text{H})+12 \sim 7.3$ . This points us to the need for further exploration toward lower mass,  $\log M_*/M_{\odot} \ll 7$ , even at such an early time of the universe, to find a less enriched galaxy system.

In Fig. 7, we show the stacked spectrum of our samples. Given that the temperature becomes high in low-metal ISM, the line ratio  $[\text{O III}]_{\lambda 4363}/[\text{O III}]_{\lambda \lambda 4959+5007}$  also becomes larger, leaving us a chance to apply the direct- $T_e$  method down to a considerably low-metallicity regime. Shown along with our stacked spectrum are a few predictions for the lines. Depending on the electron temperature, the  $[\text{O III}]_{\lambda 4363}$  line can be detected down to  $\log(\text{O}/\text{H})+12 \approx 6$  for the sensitivity enabled by JWST.

Recently, Vanzella et al. (2023) reported an upper limit of  $\log(\text{O}/\text{H})+12 < 6.3$  on a low-mass star complex ( $\lesssim 10^4 M_{\odot}$ ), through calibrated strong line methods. The system is a part of lensed arcs strongly amplified by the foreground galaxy cluster. Sub-scale observations, with an assist of strong gravitational lensing (also, Adamo et al. 2024), is a path toward the identification of pristine systems (also, e.g., Bovill et al. 2024).

Lastly, we note that the MSA slits of our NIRSPEC observations were placed near the galaxy light-center, as the default option. This is presumably the case for many other MSA programs. Given that the galaxy center is likely the place where metal enrichment is more advanced, spectroscopy of off-centered regions may also help such endeavor.

## 6. SUMMARY

In this study, we have reported 28 galaxies at  $3 < z < 9.1$  in the sightline of the cluster of galaxies MACS J1149. We detected the auroral  $[\text{O III}]_{\lambda 4363}$  line in 9 sources, which allows robust oxygen abundance determination via the direct- $T_e$  method. By combining with 16 sources from publicly available data, we found that the mass-metallicity relation exists at the redshift range of interest, with  $\sim 0.4$ - $0.7$  dex offset down below the local relation. We found that the scatter of our sources around the relation is not small. Interestingly, the deviation becomes smaller as redshift decreases, which is indirect evidence that the interplay between gravitational potential well and feedback intensity converge. We find no clear evidence of redshift evolution in our sample. While seen in previous lower- $z$  observations and predicted in simulations, we did not find the third parameter that can effectively reduce the observed scatter. Despite reaching to a considerably low-mass with an assist of strong lensing, our samples exhibit a relatively enriched ISM, indicating that the exploration of lower-mass galaxies or sub-galactic scale is needed for the search of less enriched populations, even at the redshift range explored in this study.

We investigated potential systematic impacts arising from the constraints of JWST’s MSA observations. It

is important to bear in mind that the metallicity measured using MSA slits may not necessarily represent the “global” metallicity, which is the quantity of primary concern in mass-metallicity relation analyses. This effect is likely to be more pronounced at lower redshifts or in lensing fields, where the anticipated flux loss is greater.

### ACKNOWLEDGEMENTS

We wish to thank the anonymous referee for the careful reading of the manuscript and constructive comments. Some/all of the data presented in this paper

were obtained from the Mikulski Archive for Space Telescopes (MAST) at the Space Telescope Science Institute. The specific observations analyzed can be accessed via [10.17909/q8cd-2q22](https://doi.org/10.17909/q8cd-2q22). We acknowledge support for this work under NASA grant 80NSSC22K1294. C.G., P.R., and S.S. acknowledge support through grants MIUR2017 WSCC32 and MIUR2020 SKSTHZ. KB and MT are supported by the Australian Research Council Centre of Excellence for All Sky Astrophysics in 3 Dimensions (ASTRO 3D), through project number CE170100013.

*Software:* Astropy (Astropy Collaboration et al. 2013, 2018, 2022), bbpn (Morishita 2023), EAzY (Brammer et al. 2008), EMCEE (Foreman-Mackey et al. 2013), gsf (Morishita et al. 2019), numpy (Harris et al. 2020), python-fsps (Foreman-Mackey et al. 2014), JWST pipeline (Bushouse et al. 2023).

### REFERENCES

- Adamo, A., Bradley, L. D., Vanzella, E., et al. 2024, arXiv e-prints, arXiv:2401.03224, doi: [10.48550/arXiv.2401.03224](https://doi.org/10.48550/arXiv.2401.03224)
- Andrews, B. H., & Martini, P. 2013, ApJ, 765, 140, doi: [10.1088/0004-637X/765/2/140](https://doi.org/10.1088/0004-637X/765/2/140)
- Arribas, S., Perna, M., Rodríguez Del Pino, B., et al. 2023, arXiv e-prints, arXiv:2312.00899, doi: [10.48550/arXiv.2312.00899](https://doi.org/10.48550/arXiv.2312.00899)
- Asada, Y., Sawicki, M., Abraham, R., et al. 2024, MNRAS, 527, 11372, doi: [10.1093/mnras/stad3902](https://doi.org/10.1093/mnras/stad3902)
- Astropy Collaboration, Robitaille, T. P., Tollerud, E. J., et al. 2013, A&A, 558, A33, doi: [10.1051/0004-6361/201322068](https://doi.org/10.1051/0004-6361/201322068)
- Astropy Collaboration, Price-Whelan, A. M., Sipőcz, B. M., et al. 2018, AJ, 156, 123, doi: [10.3847/1538-3881/aabc4f](https://doi.org/10.3847/1538-3881/aabc4f)
- Astropy Collaboration, Price-Whelan, A. M., Lim, P. L., et al. 2022, ApJ, 935, 167, doi: [10.3847/1538-4357/ac7c74](https://doi.org/10.3847/1538-4357/ac7c74)
- Beers, T. C., Flynn, K., & Gebhardt, K. 1990, AJ, 100, 32, doi: [10.1086/115487](https://doi.org/10.1086/115487)
- Behroozi, P., Wechsler, R. H., Hearin, A. P., & Conroy, C. 2019, MNRAS, 488, 3143, doi: [10.1093/mnras/stz1182](https://doi.org/10.1093/mnras/stz1182)
- Belfiore, F., Maiolino, R., Tremonti, C., et al. 2017, MNRAS, 469, 151, doi: [10.1093/mnras/stx789](https://doi.org/10.1093/mnras/stx789)
- Berg, D. A., James, B. L., King, T., et al. 2022, ApJS, 261, 31, doi: [10.3847/1538-4365/ac6c03](https://doi.org/10.3847/1538-4365/ac6c03)
- Bertin, E., & Arnouts, S. 1996, A&AS, 117, 393
- Bovill, M. S., Stiavelli, M., Wiggins, A. I., Ricotti, M., & Trenti, M. 2024, ApJ, 962, 49, doi: [10.3847/1538-4357/ad148a](https://doi.org/10.3847/1538-4357/ad148a)
- Boycott, K., Trenti, M., Leethochawalit, N., et al. 2024, Nature Astronomy, doi: [10.1038/s41550-024-02218-7](https://doi.org/10.1038/s41550-024-02218-7)
- Brammer, G. B., van Dokkum, P. G., & Coppi, P. 2008, ApJ, 686, 1503, doi: [10.1086/591786](https://doi.org/10.1086/591786)
- Bresolin, F. 2019, MNRAS, 488, 3826, doi: [10.1093/mnras/stz1947](https://doi.org/10.1093/mnras/stz1947)
- Bunker, A. J., Cameron, A. J., Curtis-Lake, E., et al. 2023, arXiv e-prints, arXiv:2306.02467, doi: [10.48550/arXiv.2306.02467](https://doi.org/10.48550/arXiv.2306.02467)
- Bushouse, H., Eisenhamer, J., Dencheva, N., et al. 2023, JWST Calibration Pipeline, 1.10.0, Zenodo, doi: [10.5281/zenodo.7795697](https://doi.org/10.5281/zenodo.7795697)
- Calzetti, D. 1997, AJ, 113, 162, doi: [10.1086/118242](https://doi.org/10.1086/118242)
- Campbell, A., Terlevich, R., & Melnick, J. 1986, MNRAS, 223, 811, doi: [10.1093/mnras/223.4.811](https://doi.org/10.1093/mnras/223.4.811)
- Chabrier, G. 2003, PASP, 115, 763, doi: [10.1086/376392](https://doi.org/10.1086/376392)
- Curti, M., Mannucci, F., Cresci, G., & Maiolino, R. 2020, MNRAS, 491, 944, doi: [10.1093/mnras/stz2910](https://doi.org/10.1093/mnras/stz2910)
- Curti, M., D’Eugenio, F., Carniani, S., et al. 2023a, MNRAS, 518, 425, doi: [10.1093/mnras/stac2737](https://doi.org/10.1093/mnras/stac2737)
- Curti, M., Maiolino, R., Curtis-Lake, E., et al. 2023b, arXiv e-prints, arXiv:2304.08516, doi: [10.48550/arXiv.2304.08516](https://doi.org/10.48550/arXiv.2304.08516)
- Dalmaso, N., Calabrò, A., Leethochawalit, N., et al. 2024, arXiv e-prints, arXiv:2403.11428, doi: [10.48550/arXiv.2403.11428](https://doi.org/10.48550/arXiv.2403.11428)
- Eisenstein, D. J., Johnson, B. D., Robertson, B., et al. 2023, arXiv e-prints, arXiv:2310.12340, doi: [10.48550/arXiv.2310.12340](https://doi.org/10.48550/arXiv.2310.12340)
- Faisst, A. L., & Morishita, T. 2024, arXiv e-prints, arXiv:2402.13316, doi: [10.48550/arXiv.2402.13316](https://doi.org/10.48550/arXiv.2402.13316)
- Fakhouri, O., & Ma, C.-P. 2008, MNRAS, 386, 577, doi: [10.1111/j.1365-2966.2008.13075.x](https://doi.org/10.1111/j.1365-2966.2008.13075.x)

**Table 1.** Rest-frame optical line flux measurements of  $3 < z < 9.5$  galaxies from the GTO 1199 program.

ID	[OII] <sub>3727</sub>	[NeIII] <sub>3869</sub>	[NeIII] <sub>3968</sub>	H $\delta$ <sub>4102</sub>	H $\gamma$ <sub>4340</sub>	[OIII] <sub>4363</sub>	H $\beta$ <sub>4861</sub>	[OIII] <sub>4959+5007</sub>	[NII] <sub>6548+6583</sub>	H $\alpha$ <sub>6563</sub>
GTO 1199 Sample										
30010	–	–	–	–	34.5 ± 15.0	< 11.7	63.2 ± 12.5	330.3 ± 54.7	< 71.6	147.6 ± 59.1
30055	–	–	–	47.5 ± 28.2	79.3 ± 17.9	18.8 ± 16.9	118.4 ± 16.1	1358.7 ± 102.1	< 19.3	438.3 ± 20.2
20028	–	–	63.0 ± 19.2	59.6 ± 19.0	123.6 ± 13.6	26.4 ± 9.8	267.1 ± 20.5	2061.2 ± 90.8	85.1 ± 32.9	954.4 ± 26.2
20036	–	< 6.5	< 4.6	3.7 ± 3.5	< 2.8	< 2.6	1.5 ± 1.1	12.3 ± 5.2	< 1.9	4.7 ± 1.1
150742	92.1 ± 31.2	< 19.7	< 13.2	< 11.4	< 9.3	< 14.4	31.8 ± 11.4	155.5 ± 49.7	79.8 ± 26.1	219.4 ± 12.5
20018	< 1.4	< 0.8	< 0.9	< 0.8	< 0.8	< 0.9	–	12.5 ± 2.6	< 3.4	126.2 ± 7.7
20014	–	–	–	–	–	–	–	–	< 1.4	78.5 ± 4.1
20024	104.3 ± 19.1	23.8 ± 19.4	< 27.2	47.6 ± 24.7	41.3 ± 30.2	< 20.1	183.3 ± 30.1	345.3 ± 83.4	436.8 ± 75.7	752.6 ± 37.3
20044	< 48.3	67.9 ± 38.8	< 85.7	60.7 ± 24.8	127.3 ± 38.7	< 24.2	230.5 ± 21.8	1067.2 ± 84.2	–	–
30093	100.0 ± 35.1	17.3 ± 17.1	< 29.7	< 13.4	14.5 ± 11.6	< 12.7	47.6 ± 15.5	332.7 ± 67.7	< 13.5	160.7 ± 28.1
150880	88.1 ± 12.3	52.0 ± 8.5	26.0 ± 9.4	24.6 ± 7.7	34.4 ± 6.8	11.9 ± 6.2	87.6 ± 8.2	898.7 ± 47.5	23.3 ± 11.0	286.9 ± 9.0
320108	495.6 ± 19.6	137.4 ± 12.0	74.4 ± 10.3	–	128.9 ± 5.6	13.3 ± 4.5	321.8 ± 11.9	2555.7 ± 61.7	–	–
80002	< 0.9	1.7 ± 1.1	< 1.5	1.9 ± 1.0	1.3 ± 0.5	< 0.5	–	12.4 ± 3.0	–	–
320002	8.8 ± 2.0	4.1 ± 1.6	3.5 ± 1.9	2.5 ± 1.9	4.0 ± 1.4	2.4 ± 1.9	9.5 ± 3.1	78.0 ± 15.3	< 0.7	37.6 ± 2.7
320005	82.6 ± 8.3	18.7 ± 5.2	8.1 ± 5.0	6.0 ± 3.9	16.7 ± 3.5	< 3.7	42.5 ± 5.6	363.0 ± 28.2	–	–
150903	21.2 ± 4.8	12.6 ± 3.9	5.6 ± 4.1	4.5 ± 2.2	12.0 ± 2.5	3.5 ± 2.1	17.7 ± 4.2	192.1 ± 18.5	–	–
60003	105.2 ± 26.7	30.6 ± 15.2	< 12.5	27.2 ± 19.3	19.0 ± 12.8	< 12.6	60.4 ± 30.3	254.9 ± 83.9	< 7.6	123.1 ± 32.6
10007	< 0.9	< 0.8	< 0.8	< 1.7	< 1.2	< 27.3	18.2 ± 12.6	53.8 ± 30.6	< 9.2	48.4 ± 9.2
60000	43.2 ± 6.4	12.8 ± 5.0	< 4.9	< 2.7	< 18.3	< 33.0	24.5 ± 6.9	190.0 ± 30.2	< 10.6	83.4 ± 7.7
60002	10.3 ± 6.6	< 5.6	< 1.9	–	< 6.7	< 2.5	< 0.5	< 0.5	< 0.7	< 0.6
60001	133.4 ± 12.1	28.1 ± 6.9	< 5.7	11.9 ± 5.4	27.5 ± 7.6	< 22.1	72.3 ± 8.1	569.5 ± 38.6	43.3 ± 19.3	287.9 ± 13.1
80001	< 0.2	< 0.3	< 0.6	< 0.5	< 0.5	< 0.4	< 0.3	< 0.3	< 0.5	0.8 ± 0.4
10001	3.5 ± 3.0	3.8 ± 2.3	< 1.7	4.8 ± 2.9	7.8 ± 4.0	< 2.6	–	–	–	–
10010	–	–	< 11.3	2.9 ± 1.5	6.9 ± 1.7	2.1 ± 2.1	13.6 ± 1.2	115.0 ± 6.6	< 1.5	45.9 ± 2.6
10018	< 4.1	< 5.9	5.1 ± 2.5	1.7 ± 1.4	< 3.7	< 4.1	7.6 ± 2.0	44.3 ± 8.6	< 3.4	26.5 ± 3.3
2	37.2 ± 4.1	29.9 ± 3.7	18.0 ± 3.0	13.2 ± 1.6	25.1 ± 2.4	9.9 ± 1.8	44.4 ± 4.8	561.1 ± 23.9	–	–
4	< 2.3	2.5 ± 1.6	2.9 ± 2.1	2.2 ± 1.7	2.9 ± 1.7	< 1.7	6.1 ± 1.6	33.6 ± 6.5	–	–
3	9.2 ± 2.6	15.3 ± 2.2	7.7 ± 2.2	11.0 ± 3.0	17.2 ± 2.9	6.1 ± 2.5	35.1 ± 4.4	340.6 ± 22.6	–	–
JADES sample										
18322	< 6.5	10.8 ± 6.1	16.5 ± 12.9	< 5.6	7.0 ± 4.4	4.5 ± 3.9	15.6 ± 4.1	115.3 ± 15.2	< 2.7	47.1 ± 3.8
19519	21.1 ± 5.6	9.6 ± 4.5	11.7 ± 7.3	< 5.7	5.7 ± 3.0	4.0 ± 3.6	16.3 ± 3.0	118.5 ± 11.5	< 5.7	48.9 ± 3.5
18090	18.0 ± 7.4	9.8 ± 4.3	< 6.7	< 10.3	9.2 ± 4.6	5.1 ± 4.9	25.3 ± 6.2	214.8 ± 35.2	< 9.6	69.2 ± 15.1
22251	11.3 ± 4.5	7.5 ± 3.8	< 4.7	< 7.2	< 6.4	5.6 ± 4.4	15.5 ± 3.2	127.0 ± 13.5	< 3.9	52.3 ± 4.0
18846	5.7 ± 3.8	4.7 ± 2.8	< 4.8	4.0 ± 3.6	4.8 ± 2.4	2.2 ± 2.3	14.6 ± 2.7	109.3 ± 11.6	< 5.5	56.9 ± 4.5
10058975	3.9 ± 3.0	4.6 ± 2.1	2.4 ± 2.0	< 2.0	5.8 ± 3.0	3.1 ± 3.0	13.8 ± 4.1	80.3 ± 15.9	–	–

NOTE— Fluxes are in units of  $10^{-19}$  erg/s/cm<sup>2</sup>. Flux errors and upper limits are  $3\sigma$ . Lines without the spectroscopic data coverage are marked with “–”. Texts in purple are measurements for G140M, blue for G235M, and red for G395M (and G395H for the JADES sample). The presented fluxes are not corrected for magnification nor attenuation. Fluxes for the sources from Nakajima et al. (2023) are not shown, as we adopt their published values.

**Table 2.** Physical properties of the samples

ID	R.A.	Decl.	$m_{F444W}$	$z$	$\log(\text{O}/\text{H})$	$T_e$	$AV_{\text{neb.}}$	$\log M_*$	$\log \text{SFR}$	$\mu$	$\Delta d_{\text{MSA}}$	$\Delta f_{\text{MSA}}$
	degree	degree	mag		+12	$\times 10^4 \text{ K}$	mag	$M_\odot$	$M_\odot/\text{yr}$		kpc	
GTO 1199 Sample												
30010	177.387224	22.404619	25.7	3.013	> 7.28	< 2.17	0.00	$8.81^{+0.02}_{-0.02}$	$0.7^{+0.1}_{-0.1}$	$2.1^{+0.9}_{-1.6}$	0.50	0.65
30055	177.388125	22.415668	24.9	3.214	$7.91^{+0.18}_{-0.14}$	1.58	0.98	$8.68^{+0.04}_{-0.04}$	$0.6^{+0.1}_{-0.1}$	$5.8^{+5.9}_{-1.8}$	0.24	0.66
20028	177.410476	22.419310	23.6	3.345	$7.79^{+0.07}_{-0.06}$	1.51	0.84	$9.79^{+0.01}_{-0.04}$	$1.8^{+0.1}_{-0.1}$	$1.4^{+0.1}_{-0.1}$	0.57	0.77
20036	177.392896	22.412893	28.1	3.450	> 7.15	< 3.29	–	$7.67^{+0.04}_{-0.05}$	$-0.2^{+0.1}_{-0.1}$	$3.9^{+0.1}_{-0.1}$	0.27	0.00
150742	177.429260	22.415850	23.4	3.678	–	–	–	$10.43^{+0.03}_{-0.03}$	$1.9^{+0.2}_{-0.2}$	$1.2^{+0.1}_{-0.1}$	0.66	0.78
20018	177.399186	22.384109	26.4	3.685	> 6.13	< 1.91	0.00	$8.56^{+0.07}_{-0.05}$	$0.1^{+0.1}_{-0.1}$	$1.9^{+0.1}_{-0.1}$	0.36	0.20
20014	177.391600	22.384264	27.2	3.693	–	–	–	$8.26^{+0.12}_{-0.12}$	$0.2^{+0.1}_{-0.1}$	$1.6^{+0.1}_{-0.1}$	0.49	0.07
20024	177.424202	22.386257	–	3.696	> 7.15	< 1.95	1.37	$10.23^{+0.06}_{-0.05}$	$1.8^{+0.1}_{-0.1}$	$2.1^{+0.1}_{-0.1}$	0.17	–
20044	177.383725	22.406203	25.4	3.732	> 7.49	< 1.69	0.00	$9.11^{+0.03}_{-0.03}$	$0.7^{+0.1}_{-0.1}$	$2.9^{+0.1}_{-0.1}$	0.54	0.63
30093	177.415100	22.418217	–	4.194	> 7.82	< 1.70	0.63	$9.18^{+0.04}_{-0.11}$	$1.0^{+0.1}_{-0.1}$	$1.3^{+0.1}_{-0.1}$	0.40	–
150880	177.403656	22.368355	26.6	4.247	$8.00^{+0.10}_{-0.08}$	1.49	0.50	$9.28^{+0.02}_{-0.04}$	$0.9^{+0.1}_{-0.1}$	$1.3^{+0.1}_{-0.1}$	0.29	0.41
320108	177.402573	22.384069	23.7	4.257	$8.36^{+0.05}_{-0.05}$	1.09	1.16	$10.13^{+0.01}_{-0.01}$	$1.6^{+0.1}_{-0.1}$	$2.2^{+0.1}_{-0.1}$	0.42	0.46
80002	177.394550	22.394321	28.4	4.495	> 7.50	< 1.69	0.00	$7.55^{+0.34}_{-0.25}$	$-0.6^{+0.2}_{-0.1}$	$5.7^{+0.2}_{-0.4}$	0.19	0.34
320002	177.428253	22.409452	27.5	4.658	$7.41^{+0.19}_{-0.16}$	2.59	1.24	$8.68^{+0.08}_{-0.05}$	$0.7^{+0.1}_{-0.1}$	$1.3^{+0.1}_{-0.1}$	0.19	0.39
320005	177.422580	22.414459	–	4.658	> 8.35	< 1.15	1.29	$9.60^{+0.02}_{-0.02}$	$1.4^{+0.1}_{-0.1}$	$1.3^{+0.1}_{-0.1}$	0.55	0.65
150903	177.424210	22.408874	26.4	4.659	$7.90^{+0.11}_{-0.09}$	1.68	0.00	$9.25^{+0.01}_{-0.01}$	$0.9^{+0.1}_{-0.1}$	$1.4^{+0.1}_{-0.1}$	0.16	0.34
60003	177.375739	22.399017	25.0	5.465	–	–	–	$9.19^{+0.07}_{-0.05}$	$1.1^{+0.1}_{-0.1}$	$1.7^{+0.1}_{-0.1}$	0.59	0.55
10007	177.420044	22.388666	–	5.583	–	–	–	$7.48^{+0.75}_{-0.36}$	$-0.1^{+0.2}_{-0.2}$	$3.3^{+0.1}_{-0.1}$	0.22	–
60000	177.378968	22.402419	24.4	5.585	–	–	–	$9.63^{+0.06}_{-0.06}$	$1.3^{+0.1}_{-0.1}$	$2.1^{+0.1}_{-0.1}$	0.23	0.47
60002	177.382540	22.395407	25.2	5.594	–	–	–	$9.23^{+0.08}_{-0.04}$	$1.0^{+0.1}_{-0.1}$	$2.2^{+0.1}_{-0.1}$	0.62	0.69
60001	177.412014	22.415776	24.0	5.686	> 7.69	< 2.02	1.26	$10.37^{+0.02}_{-0.02}$	$1.7^{+0.1}_{-0.1}$	$1.5^{+0.1}_{-0.1}$	0.58	0.72
80001	177.395860	22.412365	28.8	5.974	–	–	–	$6.35^{+0.66}_{-0.73}$	$-1.3^{+0.2}_{-0.1}$	$11.3^{+12.9}_{-3.8}$	0.33	0.09
10001	177.388351	22.382391	26.4	6.119	–	–	–	$9.41^{+0.01}_{-0.01}$	$0.8^{+0.1}_{-0.1}$	$1.5^{+0.1}_{-0.1}$	0.38	0.38
10010	177.412949	22.418858	25.7	6.311	$7.66^{+0.21}_{-0.16}$	1.78	0.62	$9.59^{+0.02}_{-0.03}$	$1.0^{+0.1}_{-0.1}$	$1.4^{+0.1}_{-0.1}$	0.17	0.44
10018	177.414642	22.417057	27.8	6.372	> 7.28	< 2.46	–	$8.73^{+0.03}_{-0.07}$	$0.4^{+0.1}_{-0.1}$	$1.4^{+0.1}_{-0.1}$	0.41	0.51
2	177.417709	22.417431	23.8	7.232	$7.92^{+0.04}_{-0.04}$	1.64	0.00	$9.46^{+0.02}_{-0.03}$	$1.9^{+0.1}_{-0.1}$	$1.4^{+0.1}_{-0.1}$	0.26	0.54
4	177.382950	22.412039	27.6	7.238	> 7.21	< 2.41	0.00	$7.76^{+0.12}_{-0.12}$	$-0.1^{+0.1}_{-0.1}$	$3.0^{+0.2}_{-0.1}$	0.16	0.03
3	177.389908	22.412710	25.6	9.114	$7.82^{+0.07}_{-0.07}$	1.66	0.00	$7.77^{+0.04}_{-0.02}$	$0.5^{+0.1}_{-0.1}$	$12.5^{+12.0}_{-5.0}$	0.31	0.57
JADES Sample												
18090	53.167180	–27.774615	28.2	4.769	$7.64^{+0.21}_{-0.17}$	1.93	0.00	$8.58^{+0.05}_{-0.11}$	$0.4^{+0.3}_{-0.5}$	–	0.37	0.00
18322	53.131707	–27.774119	28.4	3.153	$7.26^{+0.20}_{-0.15}$	2.78	0.43	$7.29^{+0.23}_{-0.16}$	$-0.3^{+0.3}_{-0.3}$	–	0.20	0.36
18846	53.134917	–27.772709	27.3	6.336	$7.55^{+0.22}_{-0.17}$	1.97	2.70	$8.41^{+0.08}_{-0.07}$	$0.7^{+0.1}_{-0.1}$	–	0.47	0.35
19519	53.166086	–27.771262	27.1	3.604	$7.42^{+0.21}_{-0.16}$	2.47	0.39	$8.64^{+0.08}_{-0.10}$	$0.6^{+0.1}_{-0.1}$	–	0.22	0.34
22251	53.154069	–27.766072	27.0	5.803	$7.22^{+0.18}_{-0.09}$	3.23	1.39	$7.90^{+0.22}_{-0.16}$	$0.5^{+0.1}_{-0.1}$	–	0.41	0.40
10058975	53.112434	–27.774609	27.5	9.435	$7.11^{+0.25}_{-0.15}$	2.98	1.89	$8.36^{+0.32}_{-0.19}$	$0.9^{+0.3}_{-0.1}$	–	0.27	0.00
Nakajima et al. (2023) Sample												
ERO_04590	110.859818	–73.449127	26.0	8.496	$7.09^{+0.10}_{-0.08}$	2.49	1.57	$9.05^{+0.23}_{-0.21}$	$1.1^{+0.2}_{-0.1}$	8.7	0.31	0.24
ERO_5144	110.839674	–73.445357	27.9	6.378	$7.89^{+0.09}_{-0.08}$	1.56	0.00	$8.75^{+0.13}_{-0.15}$	$1.2^{+0.8}_{-0.7}$	3.2	0.14	0.26
ERO_6355	110.844917	–73.435043	24.4	7.665	$8.29^{+0.10}_{-0.08}$	1.19	0.00	$9.07^{+0.16}_{-0.12}$	$1.5^{+0.1}_{-0.1}$	1.8	0.29	0.49
ERO_10612	110.834351	–73.435059	25.8	7.660	$7.66^{+0.06}_{-0.05}$	1.95	0.34	$8.54^{+0.17}_{-0.16}$	$1.0^{+0.1}_{-0.1}$	1.9	0.46	0.43
GLASS_100003	3.604509	–30.380444	25.1	7.877	$7.67^{+0.15}_{-0.10}$	2.00	0.00	$9.12^{+0.04}_{-0.05}$	$1.4^{+0.1}_{-0.1}$	1.3	0.43	0.40
GLASS_10021	3.608511	–30.418540	24.7	7.286	$7.88^{+0.10}_{-0.08}$	1.68	0.00	$8.69^{+0.15}_{-0.04}$	$1.6^{+0.1}_{-0.1}$	1.7	0.47	0.56
GLASS_150029	3.577166	–30.422576	26.2	4.584	$7.77^{+0.06}_{-0.05}$	1.67	0.00	$9.31^{+0.02}_{-0.03}$	$0.9^{+0.1}_{-0.1}$	1.5	0.35	0.26
GLASS_160133	3.580275	–30.424404	26.2	4.015	$8.00^{+0.05}_{-0.04}$	1.44	0.05	$8.91^{+0.02}_{-0.04}$	$0.7^{+0.3}_{-0.1}$	1.5	0.12	0.40
CEERS_01027	214.882994	52.840416	–	7.820	$7.75^{+0.17}_{-0.12}$	1.79	3.18	$9.02^{+0.13}_{-0.33}$	$1.0^{+0.1}_{-0.1}$	–	0.38	–
CEERS_01536	214.977227	52.940782	–	5.034	$7.64^{+0.13}_{-0.09}$	2.15	0.00	$8.85^{+1.19}_{-1.19}$	$1.2^{+0.2}_{-0.2}$	–	0.18	–

NOTE— †: Only those have direct metallicity measurements via  $[\text{O III}]_{\lambda 4363}$  are shown (i.e. Fig. 2). For those with upper limit on the  $[\text{O III}]_{\lambda 4363}$  flux, we derive a lower limit on  $\log(\text{O}/\text{H})$ . Errors and upper limits are  $1\sigma$ . Electron temperature ( $T_e$ ) in units of  $10^4 \text{ K}$ .

**Table 3.** Mass–Metallicity Relations of Galaxies at  $3 < z < 9.5$ . Linear Regression Best-Fit Coefficients

$N$	$\log M_0 / M_\odot$	$\alpha$	$\beta_z$	$\alpha_z$	$\sigma_{\log \text{MZR}}$
Full Sample					
34	8.8	$0.27^{+0.09}_{-0.09}$	$7.73^{+0.41}_{-0.42}$	$0.01^{+0.50}_{-0.50}$	$0.26^{+0.06}_{-0.04}$
Loss-fraction $< 0.5$					
21	8.8	$0.39^{+0.11}_{-0.11}$	$7.99^{+0.55}_{-0.54}$	$-0.33^{+0.66}_{-0.67}$	$0.27^{+0.07}_{-0.06}$

NOTE— Best-fit coefficients for the single slope regression,  $\log(\text{O}/\text{H}) = \alpha \log(M_*/M_0) + B(z)$ , where  $B(z) = \beta_z + \alpha_z \log(1+z)$ .

- Finkelstein, S. L., Bagley, M. B., Ferguson, H. C., et al. 2023, *ApJL*, 946, L13, doi: [10.3847/2041-8213/acade4](https://doi.org/10.3847/2041-8213/acade4)
- Foreman-Mackey, D., Hogg, D. W., Lang, D., & Goodman, J. 2013, *PASP*, 125, 306, doi: [10.1086/670067](https://doi.org/10.1086/670067)
- Foreman-Mackey, D., Sick, J., & Johnson, B. 2014, doi: [10.5281/zenodo.12157](https://doi.org/10.5281/zenodo.12157)
- Fukugita, M., Ichikawa, T., Gunn, J. E., et al. 1996, *AJ*, 111, 1748, doi: [10.1086/117915](https://doi.org/10.1086/117915)
- Gallazzi, A., Charlot, S., Brinchmann, J., White, S. D. M., & Tremonti, C. A. 2005, *MNRAS*, 362, 41, doi: [10.1111/j.1365-2966.2005.09321.x](https://doi.org/10.1111/j.1365-2966.2005.09321.x)
- Gardner, J. P., Mather, J. C., Abbott, R., et al. 2023, *PASP*, 135, 068001, doi: [10.1088/1538-3873/acd1b5](https://doi.org/10.1088/1538-3873/acd1b5)
- Gburek, T., Siana, B., Alavi, A., et al. 2019, *ApJ*, 887, 168, doi: [10.3847/1538-4357/ab5713](https://doi.org/10.3847/1538-4357/ab5713)
- Grillo, C., Karman, W., Suyu, S. H., et al. 2016, *ApJ*, 822, 78, doi: [10.3847/0004-637X/822/2/78](https://doi.org/10.3847/0004-637X/822/2/78)
- Hainline, K. N., Johnson, B. D., Robertson, B., et al. 2023, arXiv e-prints, arXiv:2306.02468, doi: [10.48550/arXiv.2306.02468](https://doi.org/10.48550/arXiv.2306.02468)
- Harris, C. R., Millman, K. J., van der Walt, S. J., et al. 2020, *Nature*, 585, 357, doi: [10.1038/s41586-020-2649-2](https://doi.org/10.1038/s41586-020-2649-2)
- Hashimoto, T., Laporte, N., Mawatari, K., et al. 2018, *Nature*, 557, 392, doi: [10.1038/s41586-018-0117-z](https://doi.org/10.1038/s41586-018-0117-z)
- Heintz, K. E., Giménez-Arteaga, C., Fujimoto, S., et al. 2023a, *ApJL*, 944, L30, doi: [10.3847/2041-8213/acb2cf](https://doi.org/10.3847/2041-8213/acb2cf)
- Heintz, K. E., Brammer, G. B., Giménez-Arteaga, C., et al. 2023b, *Nature Astronomy*, 7, 1517, doi: [10.1038/s41550-023-02078-7](https://doi.org/10.1038/s41550-023-02078-7)
- Henry, A., Scarlata, C., Domínguez, A., et al. 2013, *ApJL*, 776, L27, doi: [10.1088/2041-8205/776/2/L27](https://doi.org/10.1088/2041-8205/776/2/L27)
- Hoag, A., Bradač, M., Huang, K., et al. 2019, *ApJ*, 878, 12, doi: [10.3847/1538-4357/ab1de7](https://doi.org/10.3847/1538-4357/ab1de7)
- Hsiao, T. Y.-Y., Coe, D., Abdurro'uf, et al. 2023, *ApJL*, 949, L34, doi: [10.3847/2041-8213/acc94b](https://doi.org/10.3847/2041-8213/acc94b)
- Isobe, Y., Ouchi, M., Nakajima, K., et al. 2023, *ApJ*, 956, 139, doi: [10.3847/1538-4357/acf376](https://doi.org/10.3847/1538-4357/acf376)
- Izotov, Y. I., Chaffee, F. H., Foltz, C. B., et al. 1999, *ApJ*, 527, 757, doi: [10.1086/308119](https://doi.org/10.1086/308119)
- Izotov, Y. I., Stasińska, G., Meynet, G., Guseva, N. G., & Thuan, T. X. 2006, *A&A*, 448, 955, doi: [10.1051/0004-6361:20053763](https://doi.org/10.1051/0004-6361:20053763)
- Kelly, P. L., Diego, J. M., Rodney, S., et al. 2018, *Nature Astronomy*, 2, 334, doi: [10.1038/s41550-018-0430-3](https://doi.org/10.1038/s41550-018-0430-3)
- Kennicutt, Robert C., J. 1998, *ApJ*, 498, 541, doi: [10.1086/305588](https://doi.org/10.1086/305588)
- Kirby, E. N., Cohen, J. G., Guhathakurta, P., et al. 2013, *ApJ*, 779, 102, doi: [10.1088/0004-637X/779/2/102](https://doi.org/10.1088/0004-637X/779/2/102)
- Langan, I., Ceverino, D., & Finlator, K. 2020, *MNRAS*, 494, 1988, doi: [10.1093/mnras/staa880](https://doi.org/10.1093/mnras/staa880)
- Laseter, I. H., Maseda, M. V., Curti, M., et al. 2023, arXiv e-prints, arXiv:2306.03120, doi: [10.48550/arXiv.2306.03120](https://doi.org/10.48550/arXiv.2306.03120)
- . 2024, *A&A*, 681, A70, doi: [10.1051/0004-6361/202347133](https://doi.org/10.1051/0004-6361/202347133)
- Li, M., Cai, Z., Bian, F., et al. 2023, *ApJL*, 955, L18, doi: [10.3847/2041-8213/acf470](https://doi.org/10.3847/2041-8213/acf470)
- Lotz, J. M., Koekemoer, A., Coe, D., et al. 2017, *ApJ*, 837, 97, doi: [10.3847/1538-4357/837/1/97](https://doi.org/10.3847/1538-4357/837/1/97)
- Ma, X., Hopkins, P. F., Faucher-Giguère, C.-A., et al. 2016, *MNRAS*, 456, 2140, doi: [10.1093/mnras/stv2659](https://doi.org/10.1093/mnras/stv2659)
- Maiolino, R., Nagao, T., Grazian, A., et al. 2008, *A&A*, 488, 463, doi: [10.1051/0004-6361:200809678](https://doi.org/10.1051/0004-6361:200809678)
- Marino, R. A., Rosales-Ortega, F. F., Sánchez, S. F., et al. 2013, *A&A*, 559, A114, doi: [10.1051/0004-6361/201321956](https://doi.org/10.1051/0004-6361/201321956)
- Morishita, T. 2023, mtakahiro/bbnp: v1.3, v1.3, Zenodo, doi: [10.5281/zenodo.10067906](https://doi.org/10.5281/zenodo.10067906)
- Morishita, T., & Stiavelli, M. 2023, *ApJL*, 946, L35, doi: [10.3847/2041-8213/acbf50](https://doi.org/10.3847/2041-8213/acbf50)
- Morishita, T., Abramson, L. E., Treu, T., et al. 2019, *ApJ*, 877, 141, doi: [10.3847/1538-4357/ab1d53](https://doi.org/10.3847/1538-4357/ab1d53)
- Morishita, T., Roberts-Borsani, G., Treu, T., et al. 2023, *ApJL*, 947, L24, doi: [10.3847/2041-8213/acb99e](https://doi.org/10.3847/2041-8213/acb99e)
- Morishita, T., Stiavelli, M., Chary, R.-R., et al. 2024, *ApJ*, 963, 9, doi: [10.3847/1538-4357/ad1404](https://doi.org/10.3847/1538-4357/ad1404)
- Nakajima, K., Ouchi, M., Isobe, Y., et al. 2023, arXiv e-prints, arXiv:2301.12825, doi: [10.48550/arXiv.2301.12825](https://doi.org/10.48550/arXiv.2301.12825)
- Oke, J. B., & Gunn, J. E. 1983, *ApJ*, 266, 713, doi: [10.1086/160817](https://doi.org/10.1086/160817)
- Osterbrock, D. E., & Ferland, G. J. 2006, *Astrophysics of gaseous nebulae and active galactic nuclei*

- Pettini, M., & Pagel, B. E. J. 2004, *MNRAS*, 348, L59, doi: [10.1111/j.1365-2966.2004.07591.x](https://doi.org/10.1111/j.1365-2966.2004.07591.x)
- Pontoppidan, K., Blome, C., Braun, H., et al. 2022, arXiv e-prints, arXiv:2207.13067. <https://arxiv.org/abs/2207.13067>
- Postman, M., Coe, D., Benítez, N., et al. 2012, *ApJS*, 199, 25, doi: [10.1088/0067-0049/199/2/25](https://doi.org/10.1088/0067-0049/199/2/25)
- Reddy, N. A., Sanders, R. L., Shapley, A. E., et al. 2023, *ApJ*, 951, 56, doi: [10.3847/1538-4357/acd0b1](https://doi.org/10.3847/1538-4357/acd0b1)
- Sánchez-Menguiano, L., Sánchez Almeida, J., Sánchez, S. F., & Muñoz-Tuñón, C. 2023, arXiv e-prints, arXiv:2312.02046, doi: [10.48550/arXiv.2312.02046](https://doi.org/10.48550/arXiv.2312.02046)
- Sanders, R. L., Shapley, A. E., Topping, M. W., Reddy, N. A., & Brammer, G. B. 2023, arXiv e-prints, arXiv:2303.08149, doi: [10.48550/arXiv.2303.08149](https://doi.org/10.48550/arXiv.2303.08149)
- Sanders, R. L., Shapley, A. E., Kriek, M., et al. 2016, *ApJL*, 825, L23, doi: [10.3847/2041-8205/825/2/L23](https://doi.org/10.3847/2041-8205/825/2/L23)
- Sanders, R. L., Shapley, A. E., Reddy, N. A., et al. 2020, *MNRAS*, 491, 1427, doi: [10.1093/mnras/stz3032](https://doi.org/10.1093/mnras/stz3032)
- Sanders, R. L., Shapley, A. E., Jones, T., et al. 2021, *ApJ*, 914, 19, doi: [10.3847/1538-4357/abf4c1](https://doi.org/10.3847/1538-4357/abf4c1)
- Sawicki, M. 2012, *PASP*, 124, 1208, doi: [10.1086/668636](https://doi.org/10.1086/668636)
- Senchyna, P., Plat, A., Stark, D. P., & Rudie, G. C. 2023, arXiv e-prints, arXiv:2303.04179, doi: [10.48550/arXiv.2303.04179](https://doi.org/10.48550/arXiv.2303.04179)
- Shipley, H. V., Lange-Vagle, D., Marchesini, D., et al. 2018, *ApJS*, 235, 14, doi: [10.3847/1538-4365/aaacce](https://doi.org/10.3847/1538-4365/aaacce)
- Smit, R., Bouwens, R. J., Labbé, I., et al. 2016, *ApJ*, 833, 254, doi: [10.3847/1538-4357/833/2/254](https://doi.org/10.3847/1538-4357/833/2/254)
- Steidel, C. C., Strom, A. L., Pettini, M., et al. 2016, *ApJ*, 826, 159, doi: [10.3847/0004-637X/826/2/159](https://doi.org/10.3847/0004-637X/826/2/159)
- Steinhardt, C. L., Jauzac, M., Acebron, A., et al. 2020, *ApJS*, 247, 64, doi: [10.3847/1538-4365/ab75ed](https://doi.org/10.3847/1538-4365/ab75ed)
- Stiavelli, M., Morishita, T., Chiaberge, M., et al. 2023, *ApJL*, 957, L18, doi: [10.3847/2041-8213/ad0159](https://doi.org/10.3847/2041-8213/ad0159)
- Storey, P. J., & Zeppen, C. J. 2000, *MNRAS*, 312, 813, doi: [10.1046/j.1365-8711.2000.03184.x](https://doi.org/10.1046/j.1365-8711.2000.03184.x)
- Topping, M. W., Stark, D. P., Senchyna, P., et al. 2024, *MNRAS*, 529, 3301, doi: [10.1093/mnras/stae682](https://doi.org/10.1093/mnras/stae682)
- Tremonti, C. A., Heckman, T. M., Kauffmann, G., et al. 2004, *ApJ*, 613, 898, doi: [10.1086/423264](https://doi.org/10.1086/423264)
- Treu, T., Schmidt, K. B., Brammer, G. B., et al. 2015, *ApJ*, 812, 114, doi: [10.1088/0004-637X/812/2/114](https://doi.org/10.1088/0004-637X/812/2/114)
- Treu, T., Brammer, G., Diego, J. M., et al. 2016, *ApJ*, 817, 60, doi: [10.3847/0004-637X/817/1/60](https://doi.org/10.3847/0004-637X/817/1/60)
- Treu, T., Calabrò, A., Castellano, M., et al. 2023, *ApJL*, 942, L28, doi: [10.3847/2041-8213/ac9283](https://doi.org/10.3847/2041-8213/ac9283)
- Ucci, G., Dayal, P., Hutter, A., et al. 2023, *MNRAS*, 518, 3557, doi: [10.1093/mnras/stac2654](https://doi.org/10.1093/mnras/stac2654)
- Vallini, L., Witstok, J., Sommovigo, L., et al. 2024, *MNRAS*, 527, 10, doi: [10.1093/mnras/stad3150](https://doi.org/10.1093/mnras/stad3150)
- Vanzella, E., Loiacono, F., Bergamini, P., et al. 2023, *A&A*, 678, A173, doi: [10.1051/0004-6361/202346981](https://doi.org/10.1051/0004-6361/202346981)
- Venturi, G., Carniani, S., Parlanti, E., et al. 2024, arXiv e-prints, arXiv:2403.03977, doi: [10.48550/arXiv.2403.03977](https://doi.org/10.48550/arXiv.2403.03977)
- Wang, X., Jones, T. A., Treu, T., et al. 2020, *ApJ*, 900, 183, doi: [10.3847/1538-4357/abacce](https://doi.org/10.3847/1538-4357/abacce)
- Zahid, H. J., Kewley, L. J., & Bresolin, F. 2011, *ApJ*, 730, 137, doi: [10.1088/0004-637X/730/2/137](https://doi.org/10.1088/0004-637X/730/2/137)
- Zheng, W., Zitrin, A., Infante, L., et al. 2017, *ApJ*, 836, 210, doi: [10.3847/1538-4357/aa5d55](https://doi.org/10.3847/1538-4357/aa5d55)